Segmented RF shield design to minimize eddy currents for low-field Halbach MRI systems

Vos, B. de; Remis, R.; Webb, A.

Citation

Vos, B. de, Remis, R., & Webb, A. (2024). Segmented RF shield design to minimize eddy currents for low-field Halbach MRI systems. *Journal Of Magnetic Resonance*, *362*. doi:10.1016/j.jmr.2024.107669

Journal of Magnetic Resonance 362 (2024) 107669

Contents lists available at ScienceDirect

Journal of Magnetic Resonance

journal homepage: www.elsevier.com/locate/jmr

Segmented RF shield design to minimize eddy currents for low-field Halbach MRI systems

Bart de Vos [a,b,*], Rob Remis [b], Andrew Webb [a,b]

[a] *C.J. Gorter MRI center, Radiology, Leiden University Center, Leiden, The Netherlands*
[b] *Terahertz Sensing, Microelectronics, Delft University of Technology, Delft, The Netherlands*

ARTICLE INFO

Keywords:
Low-field
Shield design
Eddy currents
Halbach-array

ABSTRACT

MRI systems have a thin conducting layer placed between the gradient and RF coils, this acts as a shield at the RF-frequency, minimizing noise coupled into the experiment, and decreasing the coupling between the RF and gradient coils. Ideally, this layer should be transparent to the gradient fields to reduce eddy currents. In this work the design of such a shield, specifically for low-field point-of-care Halbach based MRI devices, is discussed. A segmented double layer shield is designed and constructed based on eddy current simulations. Subsequently, the performance of the improved shield is compared to a reference shield by measuring the eddy current decay times as well as using noise measurements. A maximum reduction factor of 2.9 in the eddy current decay time is observed. The segmented shield couples in an equivalent amount of noise when compared to the unsegmented reference shield. Turbo spin echo images of a phantom and the brain of a healthy volunteer show improvements in terms of blurring using the segmented shield.

1. Introduction

MRI systems have a thin conducting layer placed between the gradient and RF coils which acts as a shield at the RF frequency, minimizing the noise coupled into the image, and reducing the inductive coupling between the two sets of coils. This layer should sustain minimal eddy currents, created by the switching of the gradient coils, which can be the source of image artefacts [1], especially for sequences such as diffusion weighted imaging [2–5]. Eddy currents can also be a source of heating [6] and acoustic noise [7].

A substantial body of work exists for conventional high-field MRI systems with an axial B_0 field. Early patents introduced the initial designs of these shields [8–10]. Their objective was to prevent coupling between the RF body coil and the gradient coils, both situated in the bore, while minimizing eddy currents in the shield. The shields were built using flexible printed circuit board (PCB), consisting of copper–Teflon–copper layers. The thickness and permittivity of the middle layer was chosen such that the capacitance between the conductive layers resulted in a low impedance at the Larmor frequency (tens to hundreds of MHz), effectively shorting the conducting layers. However, at lower gradient switching frequencies (tens of kHz), the high impedance resulted in an open circuit. Gaps on both sides of the clad were etched to interrupt eddy current flow. To improve shielding the gaps in the conducting layers were non-overlapping such that the shield is uninterrupted at the frequency of the RF coil. The gaps were etched parallel to the conductors of the RF-transmit coil, which for the body coil on a clinical system is typically a birdcage geometry. The result was that the majority of the currents induced by the RF coil in the shield could still flow, while currents induced by the gradient coils flowing perpendicular to these gaps were interrupted. A large number of segmentations were required, ∼25 gaps were shown in the schematics on each side of the conducting clad. A more precise approach was proposed by Roemer and Edelstein [11] who used a single conducting layer. This design offers the advantage of using less material, reducing the power loss in the shield by the gradient coils. The RF currents produced in the shield were determined in an analytical manner using a Fourier decomposition of the current density. This has similarities with the target field approach proposed by Turner for gradient coil design [12]. Taking equally spaced contours of the resulting stream function [13] resulted in the locations where material was removed. An improved version was proposed by Frederick [14], which combined the streamline approach with the three layer copper–dielectric–copper embodiment. The gaps on both sides of the clad were positioned above each other. To effectively shield both quadrature modes of the transmit coil, two copper–dielectric–copper shields with an offset of 90 degrees were necessary. Subsequent innovations revealed that a single copper–dielectric–copper shield could suffice if the gaps on one side of the conducting layer were displaced by 90 degrees [15]. A

---

[*] Corresponding author at: C.J. Gorter MRI center, Radiology, Leiden University Center, Leiden, The Netherlands.
E-mail addresses: b.devos26.07@gmail.com, b.de_vos@lumc.nl (B. de Vos).

https://doi.org/10.1016/j.jmr.2024.107669
Received 24 January 2024; Received in revised form 29 March 2024; Accepted 3 April 2024

different optimization technique was proposed by Yao et al. [6]. They numerically optimized the gap locations to reduce the heating in the shield, specifically for hybrid MRI systems, and showed that cutting the shield at the cold-spots was most effective. Instead of using a solid shield, Ham and Mulder proposed a shield consisting of a conductive coating [16]. This coating was directly applied to the gradient coil unit which gives additional space and does not require a separate cooling system for the shield. This type of shield is especially effective for higher field systems where a thin layer of conducting material is sufficient to shield at the Larmor frequency.

There have been some reports regarding shielding at lower-field strengths. Bidinosti et al. [17] showed an analytical approach for actively shielded saddle RF coils, specifically for low frequency applications. The principles are similar to actively shielded gradient coils which are standard in high field systems [18–21]. This theory was then used to create a passive shield named the Faraday bracelet [22], which is a single layer shield with gaps determined by the RF coil stream lines, very similar to the approach of [11]. This shield was specifically designed for a saddle coil and tests were performed up to frequencies of 1 MHz. The shielded coil principal was also used for self-shielded polarizing coils in very low-field systems which used superconducting quantum interference devices (SQUIDS) for signal detection [23].

There are some important differences between low-field POC and conventional MRI systems, which must be considered when designing a shield. First is the transverse rather than axial direction of the B_0 field. Second, the lower Larmor frequency means an increased skin-depth, requiring more conductive material to obtain proper screening. This will lead to more eddy currents when using the same gradient fields. As an example: a 1.5 T system has an RF skin-depth in copper equal to ~8 μm, whereas at 46 mT (1.96 MHz), the skin-depth is ~6 times larger. Another downside is that the use of copper–dielectric–copper sheets is far less effective for low-field POC systems due to the impedance between the two conducting layers being inversely proportional to the frequency and the sheet dimensions. For a 46 mT system with a length of 500 mm, diameter of 300 mm, dielectric layer thickness of 125 μm and a relative permittivity of 4, the impedance between the conducting layers at the Larmor frequency is equal to ~2 Ω, which cannot be considered a short-circuit. Another difference is that conventional MRI systems have their RF-transmit body coil mounted in the bore and are therefore stationary with respect to the shield. There are also advantages when using POC low-field systems. A Halbach based system does not require a cryostat or yoke, which are know to be two major eddy current carriers. As a result the shield is potentially the primary eddy current source. This is also the reason Halbach based MRI systems do not require actively shielded gradient coils. This, in turn, increases the efficiency of the gradient coils which leads to less eddy currents for the same slew rates.

Another magnet configuration often used for POC systems are parallel plate magnets with either an H- or C-shaped yoke [24–29]. The yokes were made of a ferromagnetic material such that the magnetic flux is transferred efficiently. However, this can also be a good conductor for eddy-currents. Anti-eddy plates were used to decrease this effect, these plates were built using metals which are more resistant to eddy currents such as silicon steel [30].

In this work a multi-layer segmented RF shield is designed for a 46 mT Halbach-based low-field POC system to reduce the eddy current effects while still effectively shielding at the RF frequency. The optimal segmentation positions are determined by simulating the eddy currents in the shield and taking into account the wire pattern of the RF coil. It is shown that only a few segmentations are sufficient to significantly reduce the eddy current effects. The performance of the resulting shield is compared to an unsegmented shield using various eddy-current measurement techniques and noise characterization. Finally, the practical implications of such a shield are demonstrated using turbo spin echo (TSE) images of phantom data and a healthy volunteer.

2. Methods

The shield is designed for a 46 mT Halbach system, which uses three gradient coils designed with methods discussed in previous work [31, 32]. The RF coil used is a solenoidal head-shaped transmit/receive coil [33]. An overview of the gradient coil, RF coil and shield geometries, including their dimensions, is given in Fig. 1. The x-gradient is closest to the shield, followed by the y- and z-gradient coils.

2.1. Simulations

The gradient coil wire patterns, together with a 35 μm thick solid copper cylindrical shield are simulated using a low-frequency time-domain solver in CST Studio Suite. A smooth step function with a ramp time of 200 μs is applied to each gradient coil and the corresponding eddy-current density patterns created in the shield are observed after the ramp time. These current densities are used to determine where to place the segmentations to effectively interrupt the eddy current paths. To maintain the shielding properties, previous work suggests that segmentations should be parallel to the current density of the RF coil [8–10,14,15,22]. In this work solenoidal transmit/receive coils are used since they have optimal sensitivity for magnets with a transverse B_0 fields. The current density of these coils is primarily in the φ direction. Therefore, the segmentations are made in the φ direction, cutting through the eddy current x-component (along the bore) hot-spots. Simulations are performed before and after the segmentations.

2.2. Shield materials and construction

To validate the simulations the following setup is used. A 75 μm thick, 500 mm length clad laminate (DuPont Pyralux®) is wrapped around a 299 mm diameter, 505 mm length, 3D printed Polylactic acid (PLA) cylinder. The clad has a 35 μm thick copper layer. A soldered seam connects the two ends of the clad along the axis of the shield. The cylinder is closed at both ends using two 0.5 mm aluminum plates. The thickness of the shield is determined empirically by adding layers of the copper laminate and performing noise measurements with the RF coil and shield grounded at a central point. When multiple shielding layers are used, the conductive parts are facing outwards and the electrical connection is made via the soldered seam. When performing segmentations 2 mm gaps are used, and the shield is kept together mechanically using Kapton tape. To mitigate the noise coupled into the experiment by the introduced segmentations, a layer of 70 μm thick copper tape (40 μm copper, 30 μm conductive adhesion) is added on top of the Kapton layer and connected to one side of the segmented shield. This allows φ directed currents of the RF coil to flow where the segmentation was introduced. However, these current densities may be slightly curved due to the spiral winding of the RF coil. To deal with this, 0.1 μF capacitors are used to bridge the segmentations at multiple locations. The values of the bridging capacitors were determined by calculating the equivalent impedance using: $Z_c = \frac{1}{j\omega C}$, where C is the equivalent capacitance and ω the angular frequency of the RF or the gradients. Using 0.1 μF capacitors results in an impedance at the RF frequency which is below 0.1 Ω, while at the lower gradient frequencies the impedance will be ~200 times higher. Fig. 2 shows the segmentation, tape and capacitor strategy as discussed above.

The shield is built up step by step, introducing segmentations and performing noise measurements for each configuration. These measurements are compared to the unsegmented reference shield and the noise mitigation measures discussed above are applied if additional noise is coupled in. A value for the noise level is obtained by connecting the RF coil and acquiring a noise spectrum, i.e. no RF pulse applied, with a 50 kHz bandwidth and 256 complex data points: this was repeated 1000 times. Taking the discrete Fourier transform of these measurements results in 1000 frequency dependent noise sensitivity profiles.

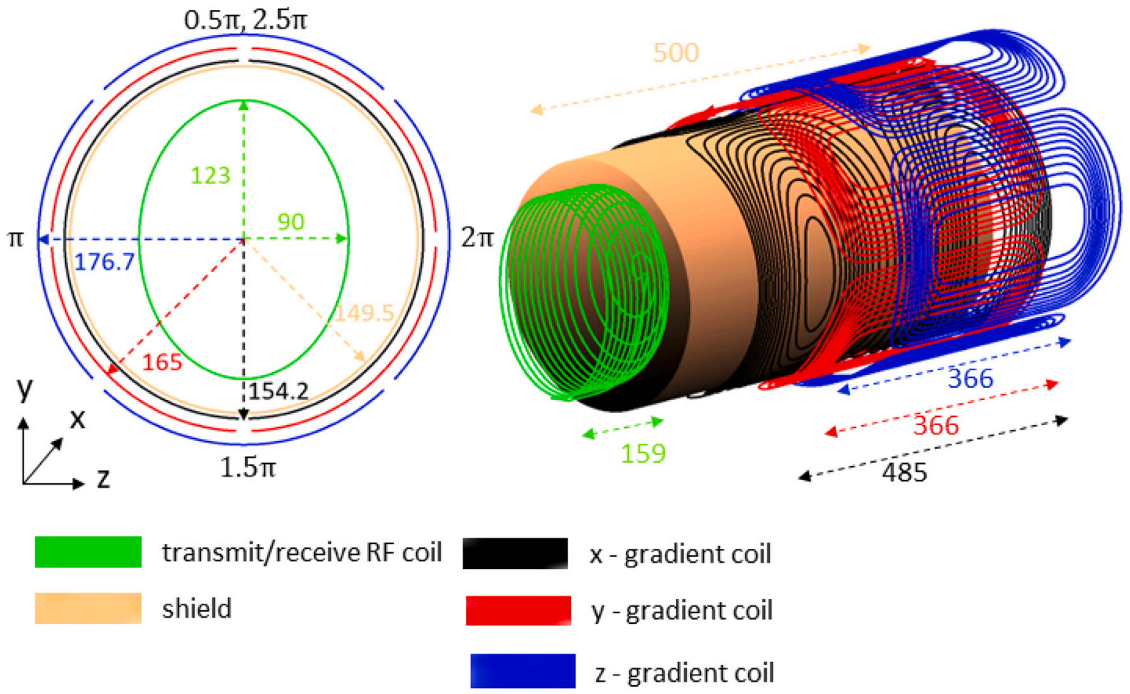

Fig. 1. Illustration of the RF coil, gradient coils and the shielding layer. Left shows a front view, right a telescopic view. Dimensions are shown in the corresponding colors, units are in mm. The left figure also shows the φ values in radians used for the 2D view of the shield. The axis system is shown in the bottom left corner of the figure. The z-direction is transverse (left–right) and corresponds to the B_0 direction, y is in the up-down direction and x is directed along the axis of the bore.

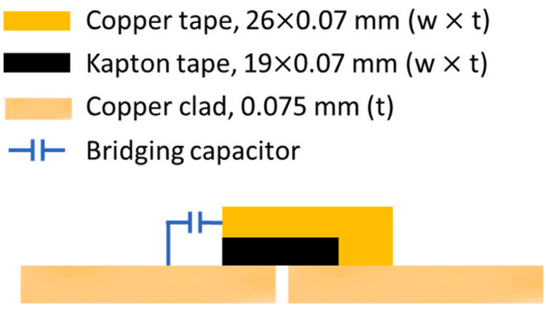

Fig. 2. Illustration of the copper clad with a segmentation, mechanically kept together while still being isolated using Kapton tape. An additional layer of copper and a bridging capacitor can be added to decrease the noise coupled into the experiment. The figure is not according to scale. The width and thickness of the materials are shown in the legend. The clad consists out of 35 μm copper, the tape has a copper thickness of 40 μm.

The standard deviation for each frequency is determined and a polynomial is fitted through the resulting profile of which the maximum value is used [34]. This is done before and after each segmentation and the subsequent noise mitigation steps. The noise measured is the background RF noise in the lab which is essentially broadband, at least within our measurement bandwidth. It consists of noise coupled in from the electrical power lines and other environmental noise produced by machinery in the hospital environment. To minimize the effects of any day-to-day fluctuations of the noise, the measurements used to compare the segmented and unsegmented shields were performed within minutes of each other.

2.3. Eddy current characteristics

Three types of measurements are used to determine the magnitude and time evolution of the eddy-currents. First, a 70 mm diameter spherical sample was placed in the center of the magnet. A 20 ms gradient pulse (x, y or z) with a 8 mT/m amplitude and ramp time of 200 μs is applied, followed by a variable delay and then a 900 readout RF pulse. The maximum of the NMR spectrum is displayed as a function of the variable delay. Second, the gradient coil interaction with the shield is determined by measuring its inductance. The mutual inductance between the shield and the coil decrease the measured inductance of the gradient coil. Therefore, more coupling results in a lower measured gradient coil inductance. As the coupling with the shield is dependent on the frequency, the inductance is measured at 0.1, 1, 10 and 100 kHz using an LCR meter. Finally the distortion of the gradient waveform is measured and compared to the input waveform. The gradient waveform used is a 10 ms pulse with a 200 μs ramp-time. The data is acquired using a small solenoidal pickup coil (100 turns, 15 × 30 mm (dxl)) connected to an oscilloscope. The pickup coil is placed at the limits of the FOV, with the axis corresponding to the gradient that is being measured. All the discussed measurements are performed using the segmented and unsegmented shield.

The practical implications of the improved shield are demonstrated by acquiring T_1 and T_2 weighted images using a 3D TSE sequences with maximum phase encoding gradients and shortest echo times. Experiments were performed on a 2D brain phantom which represents a transverse brain slab [35]. In addition, T_2 weighted images of a healthy volunteer were acquired using an echo time of 13 ms and short delay times between gradient pulses, such that the differences between the shields was most evident. Strong and short phase encoding lobes (13.6/2.8 mT/m, 770 μs) were combined with a long weak readout gradient (9.6 ms, 1.6 mT/m), resulting in a delay of 112 μs between the phase encoding and readout lobes. Furthermore, the time between the rewind phase encoding lobe and the 180°-pulse equals 433 μs. The remaining scan parameters can be found in the relevant figure caption.

3. Results

3.1. Simulations

The φ- and x-components of the simulated eddy current densities created in the shield by the individual gradient coils are shown in Fig. 3.

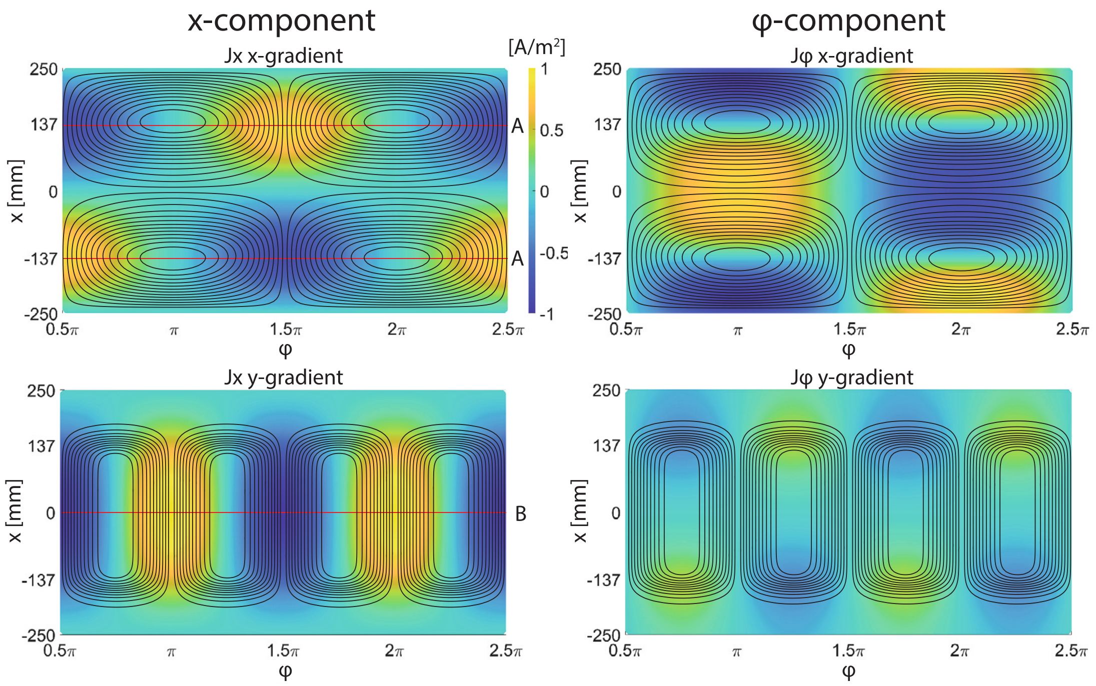

Fig. 3. The *x*- and *φ*-components of the simulated eddy current density in the shield. The currents are corrected for the gradient efficiencies and are normalized to the overall maximum value. The corresponding gradient coil wire patterns are projected on the shield. The red lines indicate the proposed segmentations through the eddy current hot spots.

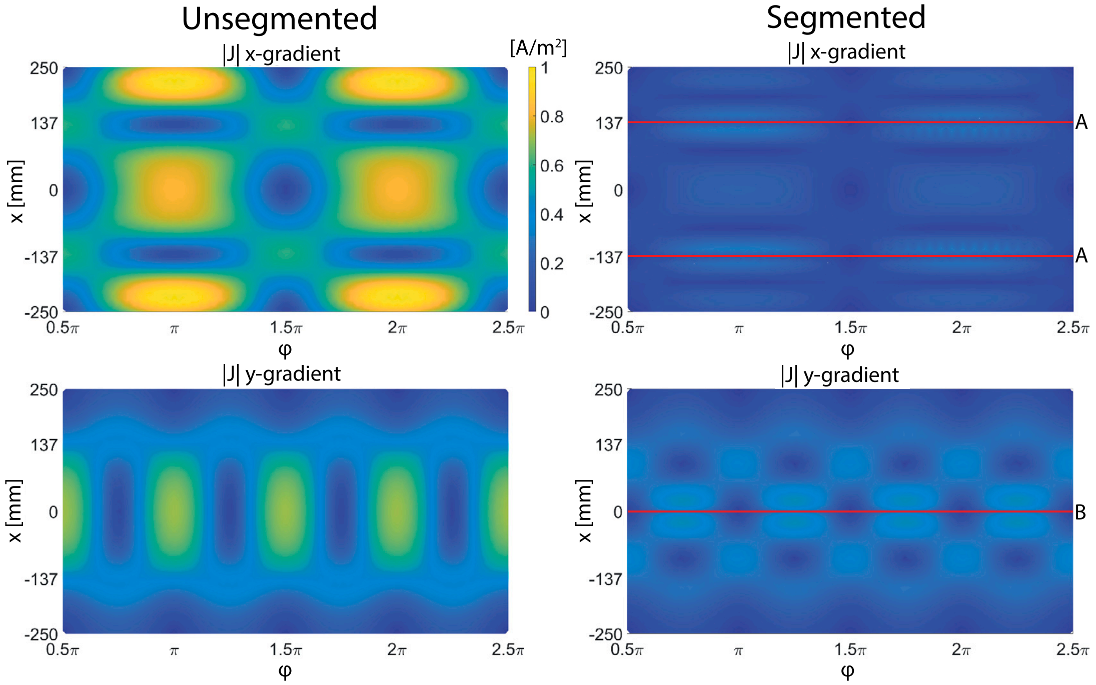

Fig. 4. Absolute value of the simulated eddy current density in the shield displayed after a 200 μs gradient ramp. The left column shows the unsegmented data, the right column the current density after the proposed segmentations (indicated with the red lines). The values are normalized to the overall maximum value and corrected for the gradient coil efficiencies.

The displayed values correspond to identical gradient field strengths (T m^{-1}), this is achieved by normalizing to the overall maximum value and correcting for the gradient coil efficiencies (T m^{-1} A^{-1}). The wire patterns are projected in the figures. The *x*-gradient is the nearest to the shield and is the least efficient, this leads to the strongest eddy current densities in the shield. The *y*- and *z*-gradient eddy currents are very similar to each other and offset by 45°. Therefore, only the simulations of the *y*-gradient coil are displayed. Less strong eddy currents are associated with these transverse gradients. Cuts are made through the maximum values of the current density *x*-component. For the *x*-gradient a segmentation at $x = \pm 137$ mm is performed, (segmentation *A*). For the transverse *z*- and *y*-gradients a segmentation at $x = 0$ mm (segmentation *B*) is made. These are indicated by the red lines in the figure. After the segmentations the simulations are rerun, the absolute value of the current densities are shown before and after the

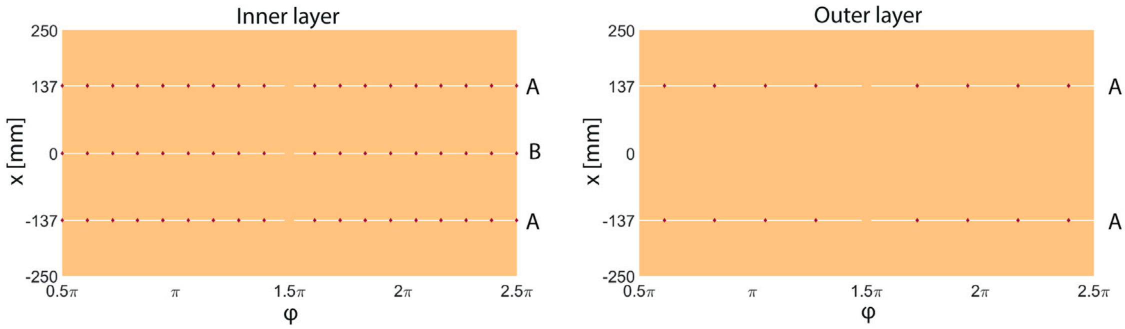

Fig. 5. Two layers of the segmented shield. The purpose of segmentation *A* is to disturb the *x*-gradient eddy currents, segmentation *B* to disturb the *y*- and *z*-gradient eddy currents. For noise purposes the outer layer does not have segmentation *B*. The red diamonds indicate the locations of the 0.1 μF capacitors used to bridge the segmentations.

segmentations in Fig. 4. To show the effect of the individual segmentations, the *x*-gradient is simulated together with a shield which has only segmentation *A*. The transverse gradients are simulated together with a shield having only segmentation *B*. Both segmentations decrease the current density. When comparing the values to the unsegmented shield, a factor of 3.2 reduction can be observed for the *x*-gradient and a factor of 1.5 and 1.45 for the *y*- and *z*-gradients. These values are measured immediately after the ramp up and therefore do not give information regarding change in decay times. The center lane at $\varphi = 1.5\pi$ is where the two parts of the sheet are soldered together and acts as a grounding lane, which is positioned directly underneath the return path of the head coil.

3.2. Shield realization and noise measurements

Two 35 μm layers are sufficient to obtain proper shielding. This is determined by adding layers of shielding, performing noise measurements and comparing the measured values to the noise floor. The noise floor is measured with a 50 ohm load connected to the spectrometer.

The segmented shield is built up by starting with a single layer and performing segmentation *A*. The noise increases by 444% compared to the situation with a single layer unsegmented shield. Adding the copper and Kapton tape as shown in Fig. 2, improves the noise to 12% above the reference value. As a final step 18 equally distributed 0.1 μF capacitors are added to bridge the segmentation, this brings the percentage down to an equivalent value as measured with a single solid shield. Subsequently, segmentation *B* is performed. The noise measured is 660% higher than the noise measured with the reference shield. After adding the copper tape this reduces to 25%. Finally, adding 18 equally spaced 0.1 μF capacitors results in a noise level 19% higher than the value measured with a single layer unsegmented shield. The second layer is added and only segmentation *A* is performed because segmentation *B* introduced too much additional noise in the single layer shield. The noise after this step is measured 36% higher than a double layer unsegmented shield. Adding the copper tape reduces the noise to 3% above the value measured with the reference shield. As a last step eight equally distributed capacitors are added bringing the noise down to the same level as the two layer unsegmented shield. The two layers of the final segmented shield are shown in Fig. 5. A Picture of the inner layer of the shield can be viewed in the supplement.

3.3. Eddy current measurements

Fig. 6 shows the results of the one pulse measurements. The results of the unsegmented reference shield are shown on the left, the segmented shield on the right. The dependence of the peak signal vs time after the gradient pulse is approximately exponential. The degree of eddy currents is clearly lower with the segmented shield. The measurements conducted with the unsegmented shield shows the MR signal has a maximum amplitude deviation compared to equilibrium, of 72, 88 and 79%, for the *x*-, *y*- and *z*-gradient coils, respectively. The segmented shield shows a maximum amplitude deviation of 1, 17 and 11% (x, y, z). The figure also shows the maximum amplitude can be reached in half the time using the segmented shield.

The results of gradient waveforms measured with the pickup coil are shown in Fig. 7. The unsegmented shield results are depicted by the solid lines. the segmented data by dotted lines. $t = 0$ is defined as the end of the ramp off time of the gradient, the input waveform is zero (black solid line). Fitting an exponential function to the unsegmented shield data results in decay times 146, 152, and 163 μs for the *x*-, *y*- and *z*- gradient coils. For the segmented shield these values are 50, 87 and 103 μs.

Fig. 8 shows the measured inductance of each gradient coil. The blue lines depict the situation with no shield in the system. In this case the inductance stays nearly constant for the measured frequencies. This indicates the coupling with other conducting structures such as the neighboring gradient coils and the RF coil at the measured frequencies is small. The orange line shows the situation using the unsegmented shield. The figure shows that between 1–100 kHz the coupling between the shield and the gradient coils greatly reduces the measured inductance. This reduction in inductance is highest for the *x*-gradient coil, namely 35% at 1 kHz compared to the case with no shield. These values are 26% and 19% for the *y*- and *z*-gradient coils. The green lines show the results for the segmented shield, clearly there is less coupling when compared the reference shield situation. Specifically, at 1 kHz: 6, 11 and 7% for the *x*-, *y*- and *z*-gradient coils. The largest improvement is observed for the *x*-gradient, which is to be expected due to segmentations *A* being present in both layers. A similar trend can be observed with the one pulse measurements and gradient waveforms: The *x*-gradient shows the biggest improvement using the segmented shield, followed by the *z*- and *y*-gradient coils. Segmentation *A* also slightly improves the performance of the *y*- and *z*-gradient coils.

3.4. Imaging results

Phantom images are shown in Fig. 9. The top row shows the T_2 weighted images, the bottom row the T_1 weighted images. As expected blurring occurs at distances far from the isocenter in the phase encoding direction: this blurring is decreased when using the segmented shield. The distortions are more evident in the T_2 weighted images, due to the longer effective echo time and larger echo train length, leading to larger phase errors propagating throughout the echo train.

Fig. 10 shows 3D TSE T_2 weighted images of a healthy volunteer. The same effects as in the phantom can be observed, the difference in blurring between the two shields is most evident for large values of $|y|$.

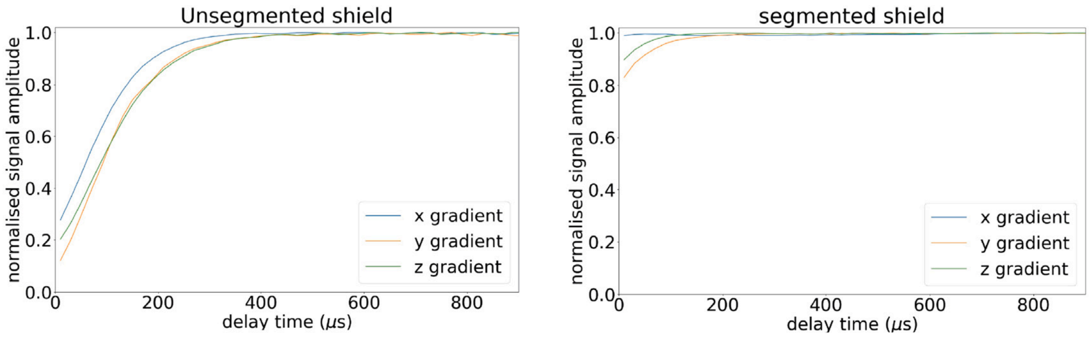

Fig. 6. Results of the one pulse measurements. The figures show the normalized maximum amplitude of the NRM spectrum as a function of delay time between the gradient lobe ramp down ($t = 0$) and the 90° RF pulse. The left figure corresponds to the unsegmented shield, the right figure to the segmented shield.

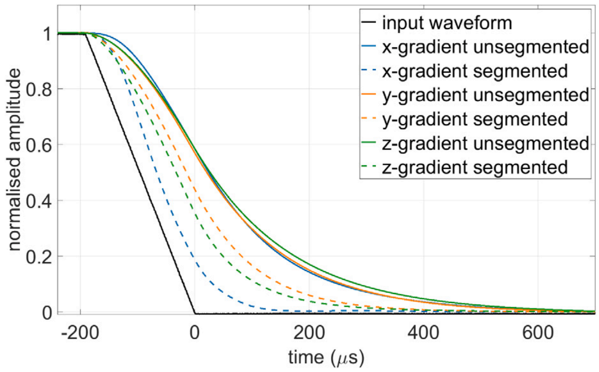

Fig. 7. Input gradient waveform measured with the voltage monitor of the amplifier (black solid line) and the output waveforms measured with a pickup coil. The solid lines shows the measurements with the unsegmented shield, the dotted lines show the segmented shield results.

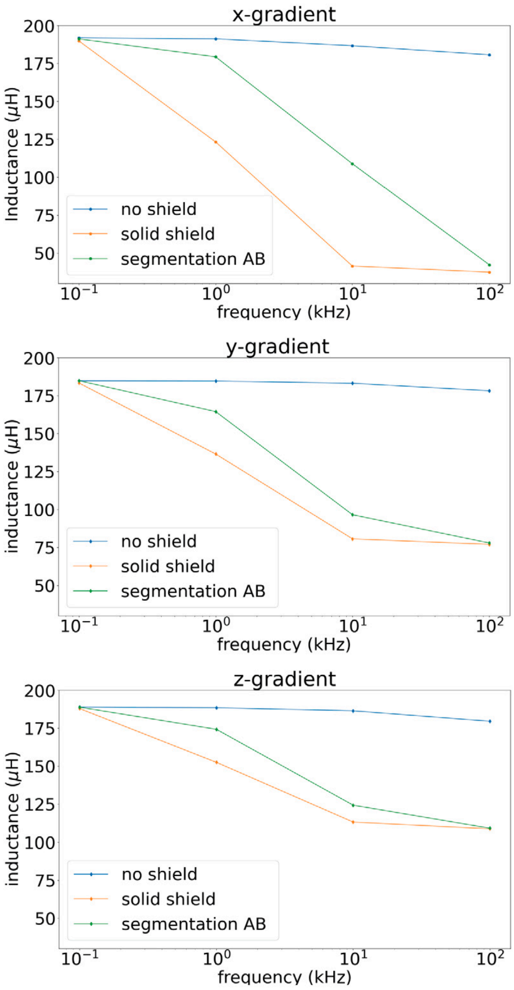

Fig. 8. The inductance of the individual gradient coils measured with a keysight U1733C, LCR meter, at 0.1, 1, 10 and 100 kHz. Three scenario's are considered: no shield in the system (blue lines), the unsegmented reference shield (orange lines), and the segmented shield (green lines).

4. Discussion

A segmented shield designed for a low-field Halbach based system was demonstrated to improve eddy current behavior compared to an unsegmented reference shield. The proposed design has a noise-shielding performance comparable to the reference shield. The relatively simple two layer shield has 5 segmentations with locations determined by electromagnetic simulations. The number of segmentations are sufficient to decrease the eddy current decay times by approximately a factor of two. Multiple techniques were used to characterize the eddy currents. A pick up coil was used to characterize the eddy current decay times, a one pulse measurement was used to investigate the influence on an FID signal, and inductance measurements were used to observe the coupling between the gradient coils and their environment.

The eddy current decay times are related to the material in which they are created. A thick material with higher conductivity is associated with longer-lived eddy currents [5]. This can also be seen from the results of the one pulse measurements using a solid shield. The signal reaches its maximum after approximately ~400 μs for a double layer shield: using a single layer shield results in this time being ~200 μs, due to half the shield thickness. Both Figs. 6 and 7 show a single dominant eddy current source (the shield) leading to a single decay constant. However, other POC systems may observe multiple eddy current components due to a shielding box, yoke or plate based gradient coils. For instance, the POC system discussed here previously had a 2 mm thick aluminum plate underneath the magnet, used for grounding purposes. This introduced long lived eddy currents in the order of 1000 μs. Figures related to this plate before and after removal are added as supplemental material. We also emphasize that the shield discussed here is designed specifically for solenoidal RF coils, noise characteristics with less-commonly used saddle or phased array coils might be quite different.

The influence of the end plates closing the cylindrical shield on the eddy currents was investigated. Inductance and one-pulse measurements performed with and without the plates revealed negligible differences. This is most probably due to the main current loops of the gradient coils being perpendicular to these conducting surfaces.

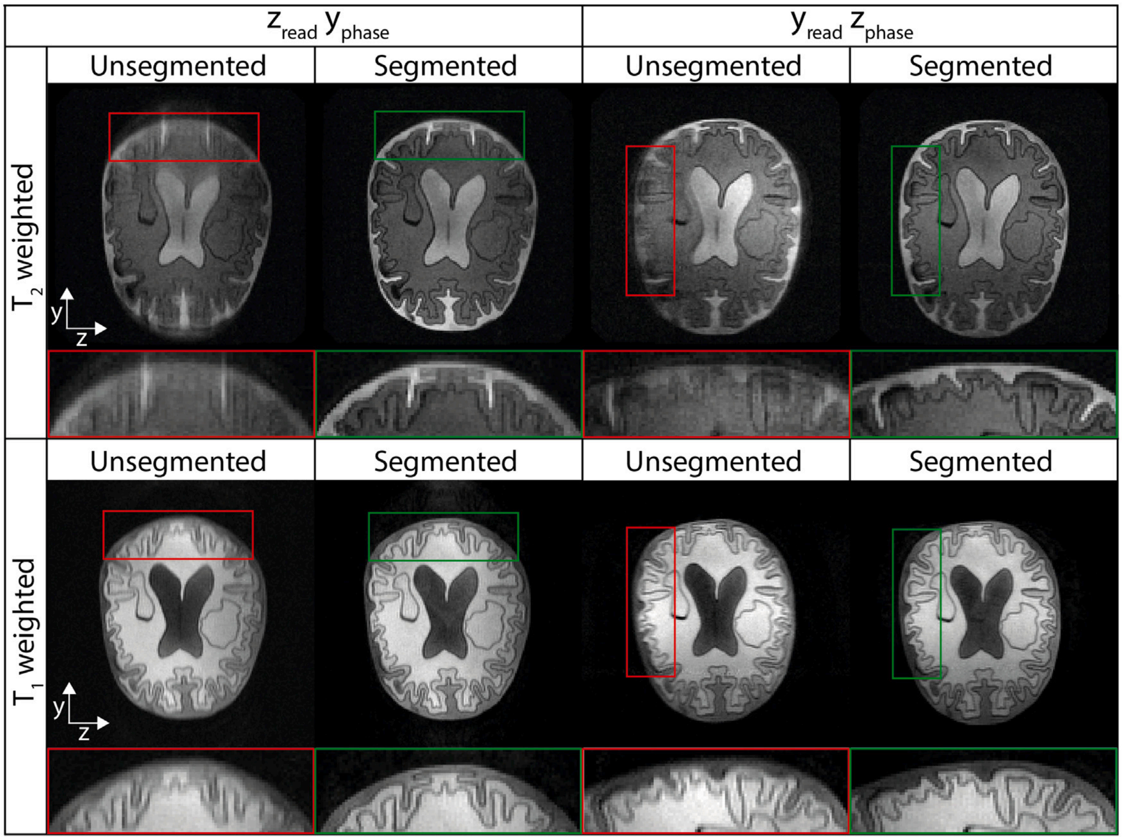

Fig. 9. T_2 and T_1 weighted images of a brain phantom. The data are obtained with the segmented and unsegmented shield. Less blurring can be observed using the segmented shield. The location of the blurring depends on the phase encoding gradient, this is shown by switching phase and frequency encoding gradients and repeating the measurements. Acquisition parameters: T_1 weighted images: BW = 29.4 kHz, FOV = 260 (z: right–left) × 260 (y: posterior–anterior) × 260 (x: head–feet) mm^3, data matrix: 346 × 173 × 3, TR/TE: 1000/15 ms, echo train length: 8, NA=1, 2x read oversampling, $|G_{max}|$ = 1.46, 13.6, 1.9 mT/m. T_2 weighted images: BW = 33.3 kHz, FOV = 240 (z: right–left) × 240 (y: posterior–anterior) × 200 (x: head–feet) mm^3, data matrix: 320 × 160 × 20, TR/TE: 2000/13 ms, echo train length: 20, 2x read oversampling, NA=1, $|G_{max}|$ = 1.6, 13.6, 1.9 mT/m (read, phase$_1$, phase$_2$).

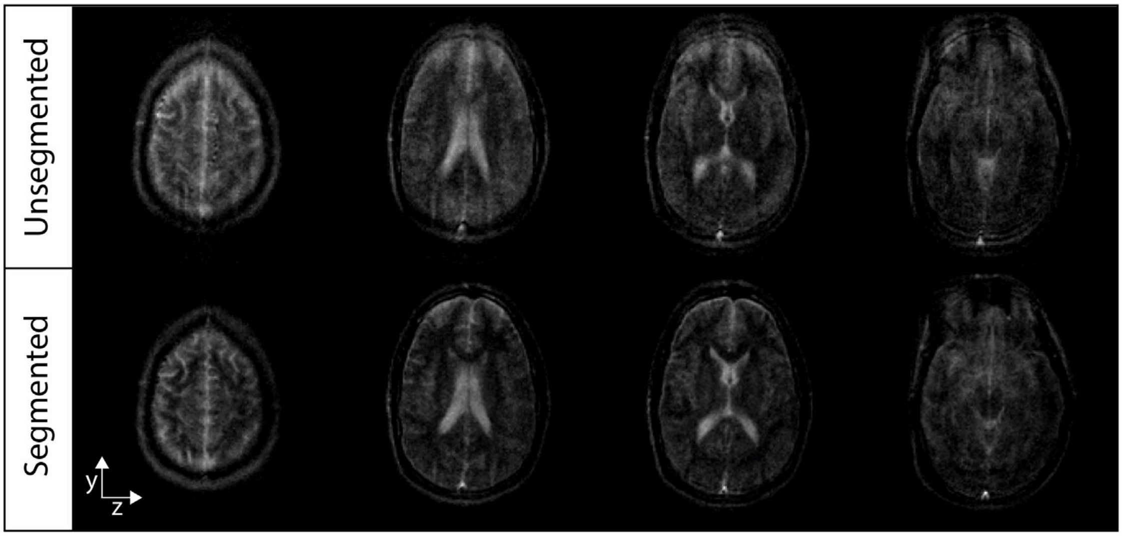

Fig. 10. T_2 weighted brain image of a healthy volunteer with the unsegmented (top row) and segmented (bottom row) shield. acquisition parameters: BW = 33.3 kHz, FOV = 240 (z: right–left) × 240 (y: posterior–anterior) × 200 (z: head–feet) mm^3, data matrix: 320 × 160 × 28, TR/TE: 2000/13 ms, echo train length: 28, NA=2, 2x readout oversampling, $|G_{max}|$ = 1.6, 13.6, 2.8 mT/m (read, phase$_1$, phase$_2$), scan duration 11 min 36 s.

In this work we created the shield using multiple layers of the copper clad. Another way to create a shield with similar characteristics would be to use a single copper sheet with twice the thickness of the clad discussed here. This could be advantageous in terms of grounding. However, it would not be possible to perform the segmentation B in only one of the layers. One could also consider using a copper–teflon–copper sheet with segmentation A on both sides and segmentation B on one side. The shield can then be constructed from a single material.

The position of the segmentation is important for the level of eddy current reduction. As a demonstration segmentation A was positioned at $x = \pm 149$, 12 mm from the original $x = \pm 137$ case. Simulations reveal this increases the maximum amplitude of the x-gradient eddy current density by 43%. The grounding lane of the shield is placed directly underneath the return path of the head coil. This is also critical, since rotating the shield 90-degrees was found to increase the noise level from 2.7 to 3.4.

Both the segmented and unsegmented shield decreases the coil Q-factor. A potential way to improve this was discussed by Kimmlingen et al. [36]. They make holes in the gradient coil holders at the locations where there are no conductors present. This creates more room for the RF flux return paths, and improves the Q-factor. This could be considered for future designs but will make the shield design more involved as it will no longer have a cylindrical geometry.

A setup which could be interesting for POC low-field systems is putting the gradient coils at the outside [37]. This could lead to a smaller magnet and thus a stronger B_0 field strength. Another advantage is that the shield can be put on the magnet exterior removing the penalty the shield has on the Q-factor of the RF coil. The major downside is that the efficiency of the gradient coils will decrease.

CRediT authorship contribution statement

Bart de Vos: Writing – review & editing, Writing – original draft, Visualization, Validation, Methodology, Formal analysis, Data curation, Conceptualization. **Rob Remis:** Writing – review & editing, Supervision, Conceptualization. **Andrew Webb:** Writing – review & editing, Project administration, Funding acquisition, Conceptualization.

Declaration of competing interest

The authors declare that they have no known competing financial interests or personal relationships that could have appeared to influence the work reported in this paper.

Data availability

Data will be made available on request.

Acknowledgments

This work was supported by ERC Advanced Grant, PASMAR, 1010 21218. The authors want to thank Tom O'Reilly for using his inductance measurement method and TSE implementation, and Chloé Najac for her trajectory used to create the T_2-weighted images.

Appendix A. Supplementary data

Supplementary material related to this article can be found online at https://doi.org/10.1016/j.jmr.2024.107669.

References

[1] C.B. Ahn, Z.H. Cho, Analysis of the eddy-current induced artifacts and the temporal compensation in nuclear magnetic resonance imaging, IEEE Trans. Med. Imaging 10 (1) (1991) 47–52, http://dx.doi.org/10.1109/42.75610.

[2] P. Jezzard, A.S. Barnett, C. Pierpaoli, Characterization of and correction for eddy current artifacts in echo planar diffusion imaging, Magn. Reson. Med. 39 (5) (1998) 801–812, http://dx.doi.org/10.1002/mrm.1910390518.

[3] N.G. Papadakis, K.M. Martin, J.D. Pickard, L.D. Hall, T.A. Carpenter, C.L. Huang, Gradient preemphasis calibration in diffusion-weighted echo-planar imaging, Magn. Reson. Med. 44 (4) (2000) 616–624, http://dx.doi.org/10.1002/1522-2594(200010)44:4<616::aid-mrm16>3.0.co;2-t.

[4] A.L. Alexander, J.S. Tsuruda, D.L. Parker, Elimination of eddy current artifacts in diffusion-weighted echo-planar images: the use of bipolar gradients, Magn. Reson. Med. 38 (6) (1997) 1016–1021, http://dx.doi.org/10.1002/mrm.1910380623.

[5] D. Le Bihan, C. Poupon, A. Amadon, F. Lethimonnier, Artifacts and pitfalls in diffusion MRI, J. Magn. Reson. Imaging 24 (3) (2006) 478–488, http://dx.doi.org/10.1002/jmri.20683.

[6] Z. Yao, Y. Wu, T. Chmielewski, S. Shvartsman, T. Eagan, M. Martens, R. Brown, Simulation guidelines for incisions patterns on RF shields, Concepts Magn. Reson. Part B: Magn. Reson. Eng. 41B (2) (2012) 37–49, http://dx.doi.org/10.1002/cmr.b.21209.

[7] W.A. Edelstein, T.K. Kidane, V. Taracila, T.N. Baig, T.P. Eagan, Y.-C.N. Cheng, R.W. Brown, J.A. Mallick, Active-passive gradient shielding for MRI acoustic noise reduction, Magn. Reson. Med. 53 (5) (2005) 1013–1017, http://dx.doi.org/10.1002/mrm.20472.

[8] C.E. Hayes, M.G. Eash, Shield for decoupling RF and gradient coils in an NMR apparatus, 1987, US Patent 4642569.

[9] R. Rzedzian, C. Martin, Split shield for magnetic resonance imaging, 1993, US Patent 5243286.

[10] P.L. Jaskolski, M.G. Eash, Mutual inductance NMR RF coil matching device, 1987, US Patent 4638253.

[11] P.B. Roemer, W.A. Edelstein, RF shield for RF coil contained within gradient coils of NMR imaging device, 1989, US Patent 4871969.

[12] R. Turner, A target field approach to optimal coil design, J. Phys. D: Appl. Phys. 19 (8) (1986) http://dx.doi.org/10.1088/0022-3727/19/8/001, L147.

[13] M.A. Brideson, L.K. Forbes, S. Crozier, Determining complicated winding patterns for shim coils using stream functions and the target-field method, Concepts Magn. Reson. 14 (1) (2002) 9–18, http://dx.doi.org/10.1002/cmr.10000.

[14] P.B. Roemer, W.A. Edelstein, Double-sided RF shield for RF coil contained within gradient coils of NMR imaging device, 1989, US Patent 4879515.

[15] P.S. Frederick, W.A. Zimmermann, P.B. Roemer, Double-sided RF shield for RF coil contained within gradient coils used in high speed NMR imaging, 1997, US Patent 5680046.

[16] C.L.G. Ham, G.B.J. Mulder, RF shield for MRI comprising conductive coating as shielding material, 2016, US Patent 9417301.

[17] C.P. Bidinosti, I.S. Kravchuk, M.E. Hayden, Active shielding of cylindrical saddle-shaped coils: Application to wire-wound RF coils for very low field NMR and MRI, J. Magn. Reson. 177 (1) (2005) 31–43, http://dx.doi.org/10.1016/j.jmr.2005.07.003.

[18] R. Turner, R.M. Bowley, Passive screening of switched magnetic field gradients, J. Phys. E: Sci. Instrum. 19 (10) (1986) 876, http://dx.doi.org/10.1088/0022-3735/19/10/023.

[19] P. Mansfield, B.L.W. Chapman, R. Turner, R.M. Bowley, Magnetic field screens, 1990, US Patent 4978920.

[20] B. Chapman, P. Mansfield, Double active magnetic screening of coils in NMR, J. Phys. D: Appl. Phys. 19 (7) (1986) L129, http://dx.doi.org/10.1088/0022-3727/19/7/001.

[21] B.L.W. Chapman, Shielded gradients. And the general solution to the near field problem of electromagnet design, MAGMA 9 (3) (1999) 146–151, http://dx.doi.org/10.1007/BF02594613.

[22] C.P. Bidinosti, M.E. Hayden, Selective passive shielding and the Faraday bracelet, Appl. Phys. Lett. 93 (17) (2008) 174102, http://dx.doi.org/10.1063/1.2998607.

[23] J.O. Nieminen, P.T. Vesanen, K.C.J. Zevenhoven, J. Dabek, J. Hassel, J. Luomahaara, J.S. Penttilä, R.J. Ilmoniemi, Avoiding eddy-current problems in ultra-low-field MRI with self-shielded polarizing coils, J. Magn. Reson. 212 (1) (2011) 154–160, http://dx.doi.org/10.1016/j.jmr.2011.06.022.

[24] M. Nakagomi, M. Kajiwara, J. Matsuzaki, K. Tanabe, S. Hoshiai, Y. Okamoto, Y. Terada, Development of a small car-mounted magnetic resonance imaging system for human elbows using a 0.2 T permanent magnet, J. Magn. Reson. 304 (2019) 1–6, http://dx.doi.org/10.1016/j.jmr.2019.04.017.

[25] Y. He, W. He, L. Tan, F. Chen, F. Meng, H. Feng, Z. Xu, Use of 2.1 MHz MRI scanner for brain imaging and its preliminary results in stroke, J. Magn. Reson. 319 (2020) 106829, http://dx.doi.org/10.1016/j.jmr.2020.106829.

[26] K.N. Sheth, M.H. Mazurek, M.M. Yuen, B. Cahn, J.T. Shah, A. Ward, J.A. Kim, E.J. Gilmore, G.J. Falcone, N. Petersen, K.T. Gobeske, F. Kaddouh, D.Y. Hwang, J. Schindler, L. Sansing, C. Matouk, J. Rothberg, G. Sze, J. Siner, M.S. Rosen, S. Spudich, W.T. Kimberly, Assessment of brain injury using portable, low-field magnetic resonance imaging at the bedside of critically ill patients, JAMA Neurol. 78 (1) (2021) 41–47, http://dx.doi.org/10.1001/jamaneurol.2020.3263.

[27] M.H. Mazurek, B.A. Cahn, M.M. Yuen, A.M. Prabhat, I.R. Chavva, J.T. Shah, A.L. Crawford, E.B. Welch, J. Rothberg, L. Sacolick, M. Poole, C. Wira, C.C. Matouk, A. Ward, N. Timario, A. Leasure, R. Beekman, T.J. Peng, J. Witsch, J.P. Antonios, G.J. Falcone, K.T. Gobeske, N. Petersen, J. Schindler, L. Sansing, E.J. Gilmore, D.Y. Hwang, J.A. Kim, A. Malhotra, G. Sze, M.S. Rosen, W.T. Kimberly, K.N. Sheth, Portable, bedside, low-field magnetic resonance imaging for evaluation of intracerebral hemorrhage, Nature Commun. 12 (1) (2021) 5119, http://dx.doi.org/10.1038/s41467-021-25441-6.

[28] B. Cahn, J. Shah, H. Dyvorne, R. O'Halloran, M. Poole, M. Yuen, M. Mazurek, A. Ward, S. Payabvash, R. Beekman, S. Brown, G. Falcone, K. Gobeske, N. Petersen, A. Jasne, R. Sharma, J. Schindler, L. Sansing, E. Gilmore, C. Wira, C. Matouk, G. Sze, M. Rosen, W.T. Kimberly, K. Sheth, Deployment of Portable, Bedside, Low-field Magnetic Resonance Imaging for Evaluation of Stroke Patients (272), Neurology 94 (2020) 272.

[29] Y. Liu, A.T.L. Leong, Y. Zhao, L. Xiao, H.K.F. Mak, A.C.O. Tsang, G.K.K. Lau, G.K.K. Leung, E.X. Wu, A low-cost and shielding-free ultra-low-field brain MRI scanner, Nature Commun. 12 (1) (2021) 7238, http://dx.doi.org/10.1038/s41467-021-27317-1.

[30] M.S. Poole, C. Hugon, H.A. Dyvorne, L. Sacolick, W.J. Mileski, J.C. Jordan, A.B.K. Jr., J.M. Rothberg, T. Rearick, C.T. McNulty, Electromagnetic shielding for magnetic resonance imaging methods and apparatus, 2019, US Patent 10274561.

[31] B. de Vos, J. Parsa, Z. Abdulrazaq, W.M. Teeuwisse, C.D.E. Van Speybroeck, D.H. de Gans, R.F. Remis, T. O'Reilly, A.G. Webb, Design, Characterisation and Performance of an Improved Portable and Sustainable Low-Field MRI System, Front. Phys. 9 (2021) http://dx.doi.org/10.3389/fphy.2021.701157.

[32] B. de Vos, P. Fuchs, T. O'Reilly, A. Webb, R. Remis, Gradient coil design and realization for a Halbach-based MRI system, IEEE Trans. Magn. 56 (3) (2020) 1–8, http://dx.doi.org/10.1109/TMAG.2019.2958561.

[33] T. O'Reilly, W.M. Teeuwisse, D. de Gans, K. Koolstra, A.G. Webb, In vivo 3D brain and extremity MRI at 50 mT using a permanent magnet Halbach array, Magn. Reson. Med. 85 (1) (2021) 495–505, http://dx.doi.org/10.1002/mrm.28396.

[34] A. Webb, T. O'Reilly, Tackling SNR at low-field: a review of hardware approaches for point-of-care systems, Magn. Reson. Mater. Phys. Biol. Med. 36 (3) (2023) 375–393, http://dx.doi.org/10.1007/s10334-023-01100-3.

[35] B. de Vos, R.F. Remis, A.G. Webb, Characterization of concomitant gradient fields and their effects on image distortions using a low-field point-of-care Halbach-based MRI system, Magn. Reson. Med. 91 (2) (2024) 828–841, http://dx.doi.org/10.1002/mrm.29879.

[36] R. Kimmlingen, R. Lazar, J. Nistler, W. Renz, M. Vester, Magnetic resonance apparatus with an RF antenna unit and a gradient coil unit, 2007, US Patent 7230427.

[37] B. de Vos, R.F. Remis, A.G. Webb, An integrated target field framework for point-of-care halbach array low-field MRI system design, Magma (New York, N.Y.) 36 (3) (2023) 395–408, http://dx.doi.org/10.1007/s10334-023-01093-z.